Particle organization after viscous sedimentation in tilted containers

Sergio Palma,[1,2,a)] Christian F. Ihle,[3,1,b)] Aldo Tamburrino,[4,1] and Stuart B. Dalziel[2]

[1)] *Advanced Mining Technology Center, University of Chile, Chile.*

[2)] *Department of Applied Mathematics and Theoretical Physics, University of Cambridge, United Kingdom.*

[3)] *Department of Mining Engineering, University of Chile, Chile.*

[4)] *Department of Civil Engineering, University of Chile, Chile.*

(Dated: 28 June 2016)

A series of sedimentation experiments and numerical simulations have been conducted to understand the factors that control the final angle of a static sediment layer formed by quasi-monodisperse particles settling in an inclined container. The set of experiments includes several combinations of fluid viscosity, container angle and solids concentration. A comparison between the experiments and a set of two-dimensional numerical simulations shows that the physical mechanism responsible for the energy dissipation in the system is the collisions between the particles. The results provide new insights into the mechanism that sets the morphology of the sediment layer formed by the settling of quasi-monodisperse particles onto the bottom of an inclined container. Tracking the interface between the suspension solids and the clear fluid zone reveals that the final angle adopted by the sediment layer shows strong dependencies on the initial particle concentration and the container inclination, but not the fluid viscosity. It is concluded that (1) the hindrance function plays an important role on the sediment bed angle, (2) the relation between the friction effect and the slope may be explained as quasi linear function of the projected velocity along the container bottom, and (3) prior to the end of settling there is a significant interparticle interaction through the fluid affecting to the final bed organization. We can express the sediment bed slope as a function of two dimensionless numbers, a version of the inertial number and the particle concentration. The present experiments confirm some previous results on the role of the interstitial fluid on low Stokes number flows of particulate matter.

PACS numbers: Valid PACS appear here

Keywords: Suggested keywords

[a)] Corresponding author: sergio.palma@ing.uchile.cl

[b)] Corresponding author: cihle@ing.uchile.cl

I. INTRODUCTION

Sedimentation is a process by which solid particles are separated from a fluid under the action of the gravitational force. Such a process is one of the oldest known techniques used in petroleum, pharmaceutical, mining and chemical industry to clean fluids or, alternatively, to recover solid particles[10,19]. The sedimentation of particles at high concentrations has been studied from a kinematic perspective in the context of vertical gravitational settlers[3,25]. Differently from the case of settling in upright containers, where fluid-particle and interparticle interactions can be expressed as a function of the local concentration only[10], settling on inclined planes also depends on local shear[1,21,32]. The impact of shear on particle dynamics in confined or inclined geometries can be further amplified by shear-induced diffusion occurring at sufficiently high particle sizes and concentrations[26,32]. The settling process at high concentrations has been studied in the context of sheared Couette cells as effectively Newtonian fluids [26,32], and also to explain the flow and particle organization process in flows over inclined planes with a constant particle supply[23,30]. In particular, the flow of a sediment layer that forms on an inclined surface as a consequence of the steady sedimentation of monodisperse spherical particles was investigated experimentally and theoretically by Kapoor and Acrivos[23]. They modified the model proposed by Nir and Acrivos[30] to include shear-induced diffusion due to gradients in the shear stress as well as a slip velocity along the wall due to the finite size of the particles.

When sedimentation occurs in an upright container with vertical walls and a horizontal bottom, particles tend to be distributed in horizontal layers according to their size and relative volume fractions (e.g. Davis and Acrivos[10]). In contrast with upright containers, iso-concentration lines are not necessarily aligned with an inclined lower boundary for the container and have been found to follow a power law of the bottom coordinate[23,30].

A related boundary-induced flow is driven by the Boycott effect, which results in the enhancement of the sedimentation process due to the presence of an inclined upper boundary in the system that creates a clear fluid layer on top that accelerates the settling compared to the upright situation, where particles must settle over the entire depth into the bottom in a container with vertical walls. Around 30 years ago there were several investigations (e.g. Acrivos and Herbolzheimer[1], Herbolzheimer and Acrivos[21], Leung and Probstein[27], Shaqfeh and Acrivos[35]) that examined theoretically the flow fields within the various zones of inclined geometries. Such researchers derived analytic expressions for the velocity profiles within the clear fluid layer underneath the downward facing wall and within the suspension for a wide range of parameters. The formation and flow of the sediment layer on the upward facing surface was neglected in most of these studies. Leung and Probstein [27] studied the sediment layer as an effective Newtonian fluid, but since no theory was available for determining the volume fraction of particles within the flowing concentrated sediment, such a model assumed a stepwise particle concentration distribution.

Particle settling in viscous fluids upon inclined planes has been extensively investigated for small Stokes and particle Reynolds numbers[21,23,31]. Motivated by the study of submarine granular flows, Cassar et al. [4] have focused on the dense flow regime occurring when the whole sediment layer is flowing down the slope and when no deposition occurs[4]. They studied the variation of the mean velocity and the pore pressure below the avalanche as a function of the two control parameters, the surface inclination and the layer thickness. Such results were analysed using a theoretical model obtained from dry granular flows substituting the inertial time scale by a viscous time scale. Their model was expressed in terms of a so-called inertial number[14], a dimensionless ratio of time scales that we shall employ in our interpretation of results.

Courrech du Pont et al. [7] have suggested that granular avalanches can flow according to three different regimes depending on the time scale associated to the particle motion in the fluid. In particular, prior to the collision of a single particle with a neighbour, the particle may have not reached its terminal velocity, thus defining the free-fall regime. If the terminal velocity has been reached, it can be within a viscous or an inertial regime, depending on the balance of forces. The parameters controlling these dynamics are the Stokes number, the particle to fluid density ratio, and the particle Reynolds number. In particular, for small values of the Stokes number, they confirm the previous observation that the presence of a viscous fluid has the ability to exhaust the available kinetic energy after collisions, rendering them inelastic[18,22]. This is a key element to understanding the particle and fluid dynamics of dense mixtures flowing in liquids confined in rotating cylinders and on inclined planes. On one hand, the settling in an initially homogeneous suspension in an inclined container may be effectively the same as that in an upright container away from the bottom, where particle hindrance is a dominant effect during the settling. This behaviour has been observed in thickeners and clarifiers, whose bottom is often conical[6]. On the other hand, those particles moving near the inclined boundary may experience close interactions via the interstitial fluid or direct contacts, which may cause particle velocity gradients. The result of these three stages with different dynamics form a particle bed that is not parallel to the bottom.

In the present paper, we study the final shape of the particle bed within a large inclined container by means of numerical simulations and experiments. The particle motion is in the viscosity-dominated regime, and thus the particle Reynolds number, and the Stokes number, are small. We seek a relation between the angle of inclination of the container and the angle of the surface of the particle bed. The aforementioned flow characteristics —both away from and close to the sediment layer— are captured using scaling arguments to explain the prevailing mechanisms that control the final bed organization. In Section II, we detail the experimental procedure used to track the interface between the suspension and the clear region and measure the final angle of inclination of the sediment layer. Also, we present the mathematical model and the numerical procedure used for the numerical simulations. In Section III, we discuss the results of our experiments and numerical simulations, and conclude in Section IV.

II. MATERIALS AND METHODS

A. Experiments

The experimental set-up is shown schematically in Fig. 1(a) and consists of an inclined transparent acrylic settling container of $25 \times 21 \times 3\,\mathrm{cm}^3$ (width $\times$ height $\times$ thickness) filled with an initially homogeneous suspension of negatively buoyant spheres in a viscous liquid. We considered different combinations of initial particle concentration (ϕ_0), container inclination angle measured from the horizontal plane (θ_s), and liquid viscosity (η_f).

A solution of glycerine ($C_3H_8O_3$) and water was used in all experiments. The glycerine concentrations ranged from 45% to 55% by volume, resulting in dynamic viscosities between 6.30 ± 0.08 mPa·s and 11.48 ± 0.15 mPa·s, and densities between $1.13 \pm 0.02\,\mathrm{g/cm}^3$ and $1.16 \pm 0.02\,\mathrm{g/cm}^3$, [5]. For all the experiments we kept the fluid at 20°C, and thus controlled both the density and viscosity with the glycerine concentration.

The particles used were spherical, partially translucent resin beads (Purolite® PCR833 Gel SAC - Special Grading, Na+ Form) with radius $a = 125 \pm 13\,\mu\mathrm{m}$ and density $\rho_s =$

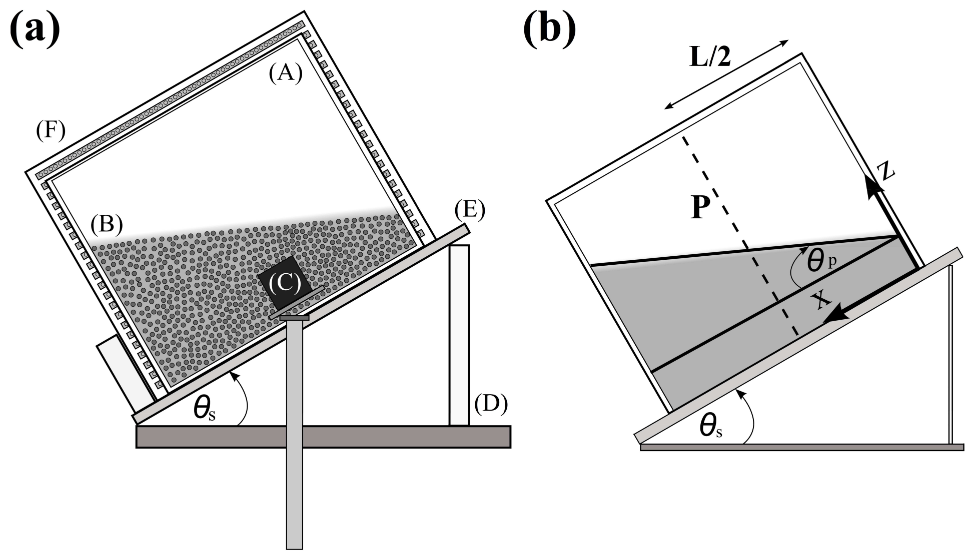

FIG. 1. (a) Schematic of the experimental setup. (A): acrylic container, (B): resin beads, shown in grey, (C): video camera, (D): adjustable lab jack, (E): inclined support, (F): LED back lighting. (b) General configuration of the problem. In all the experiments, the camera is aligned with the bottom of the tank. The angle of the sediment layer measured respect to the base of the container is θ_p.

$1.31 \pm 0.07\,\mathrm{g/cm^3}$. We measured a loose packing volume fraction of 0.61 ± 0.02, close to that expected for monodisperse spheres. We estimated this value by measuring the volume of water displaced when a known volume of packed particles was immersed in water. We measured the angle of repose of the dry particles with respect to the horizontal plane, $\theta_d = 19.9^\circ \pm 0.3^\circ$. This has been measured as the cone angle obtained after releasing the particles from a height of 15 cm on a rough surface made of the same particles, stuck to the bottom, horizontal plane. This experiment has been repeated 20 times to obtain statistical convergence. The parameter θ_d has been used as a reference to define the reservoir inclination angles from 0 to $1.51\theta_d$, the former case corresponding to a horizontal sediment layer.

We illuminated the flow trough an acrylic diffuser using a 24 W cool white LED panel consisting of 200 emitters giving a diffusive backlighting without significant heating. In the present measurements we used an 8-bit, 12 frames/sec UniqVision UP900DS-CL RGB camera with a spatial resolution of 640×480 pixels^2, to record a region of $25 \times 14\,\mathrm{cm}^2$. This region excludes a 7 cm length band at the top of the tank. Although the camera's resolution precluded the use of pattern matching algorithms to obtain the downslope component of the

TABLE I. Set of experimental conditions.

	Values
System angle θ_s (°), ± 0.5°	$[0, 10, 20, 30]$
Fluid viscosity η_f (mPa·s), ± 1.3%	$[6.30, 7.25, 8.40, 9.78, 11.48]$
Initial volume fraction ϕ_0 (%), ±0.1%	$[5.0, 7.5, 10.0, 12.5, 15.0, 17.5, 20.0]$

particle velocity field, it allowed the measurement of the location of the solids interface with considerable accuracy, as was later verified with the output of the numerical simulations. The length of influence of the walls have been found to be of about 5 cm, whereas the edges of the interrogation windows are at a minimum distance of 10 cm from the walls. In addition, we have attached black tape to the bottom of the tank, where the transparent acrylic walls are joined, in order to minimize the light penetration from the walls into the particles. The image post-processing was undertaken with DigiFlow ver 3.4[9]. We conducted a total of 140 experiments, exploring all different combinations of 4 inclination angles, 5 fluid viscosities and 7 particle volume fractions, as listed in Table I.

The procedure for each experiment is summarized as follows. The empty container was positioned on top of the inclined surface after this had been carefully set an angle of θ_s, with the same angle set for the camera. The suspension, previously stored in a beaker, is then poured into the inclined container. Immediately after, it was gently agitated for 2 min to keep the particles in suspension while allowing bubbles to rise to the surface. To minimize air entrainment, this step was undertaken avoiding sloshing or splashing of the mixture. We have tested the initial homogeneity of the suspension comparing different concentration profiles along the x axis for the case $\theta_s = 0$. We started the video recording during the mixing process to ensure the whole settling experiment was captured. The particle settling process in the system with an inclined container took between 60 s and 240 s, depending on the glycerin/particle concentration combination. The settling process finally evolved into the formation of a sediment layer, whose upper surface was found to be approximately linear in most of the experiments (see Fig. 8, Section III). Previous work[23] has suggested that the sediment layer can be modelled by, $h(x) \sim x^a$, $a \leq 1$, with the coordinate x aligned with the tank bottom. The present set of experiments showed that $a \approx 1$ gives a reasonable approximation of the finally settled condition in the central region of the container. This allows a simple description of the settled bed using a uniform slope as a relevant single parameter. Once the settling process was completed, the sediment layer formed an angle $\theta = \theta_s - \theta_p$ with respect to the horizontal, where, θ_p is the angle measured from the base of the container, as depicted in Fig. 1(b). This angle was determined using linear regression on measurements of the height of the interface between the fluid and the sediment layer. The angle θ was, in general, less and equal to the angle of repose θ_d. The back lighting of the translucent particles in these quasi-two-dimensional experiments allowed the transmitted light intensity to be related to the particle concentration.

Fig. 2 shows the experimental calibration curve obtained from the volume fraction of particles as a function of the mean normalized transmitted light intensity over the container, $\overline{i_n} = (1/NM)\sum_j \sum_k i_n(j,k)$, where i_n is the light intensity at the nodes i and j, with $1 \leq i \leq N$ and $1 \leq j \leq M$. Here, N and M correspond to the vertical and horizontal number of nodes in the measurement window, respectively. The calibration experiment consisted of relating the mean normalized intensity of light at $t = 0$ in a centred 60×60 mm^2 window, with the mean concentration of particles, measured by a mass balance. We repeated these steps for different concentrations of particles and fluids. Each experiment was repeated three times. A relation between concentration and the normalized mean intensity over the container, $\overline{i_n}$, is given by the empirical fit

$$\phi = \alpha_1 \overline{i_n}^{\,\alpha_2} + \alpha_3 \overline{i_n} + \alpha_4 \tag{1}$$

We determined the coefficients α_1 to α_4 using a Levenberg-Marquardt algorithm[29], the results of which are given in Table II. In the same figure, the inset shows the mean normalized transmitted light intensity as a function of the vertical axis in a calibration experiment using a vertical container, for a viscosity of $\eta_{f1} = 6.30 \pm 0.08$ mPa·s and an initial volume fraction of $\phi_0 = 5.0 \pm 0.1$ %. The profile corresponds to the final state of the particle sedimentation.

TABLE II. Fit coefficients for light intensity function (1). The values Δ_{α_j} represent the corresponding fit errors. The obtained correlation coefficient for the fit parameters is $R^2 = 0.9998$.

Values	1	2	3	4
α_j	0.0080	-2.21	-33.50	33.50
Δ_{α_j}	0.0001	0.01	0.01	0.01

For each initial volume fraction, vertical profiles of the light intensity (taken as the Euclidean norm of the RGB vector of the pixel values) were determined at 25 evenly spaced locations along the horizontal axis of the acrylic container. These profiles were then averaged and normalized to yield the transmitted light. The grey line represents the mean normalized intensity profile $i_n(z)$ and the black lines correspond to the fluctuations in the concentration profiles. It shows that the scatter is small compared to the mean profile obtained.

The mean normalized transmitted light intensity over the container $\overline{i_n}$ has an error of 1% for $\overline{i_n} > 0.20$ and 0.3% for $\overline{i_n} \leq 0.20$. The corresponding uncertainties have been calculated as the standard deviation of intensity curves corresponding to the 25 light intensity profiles. This calibration allowed us to determine the concentration of quasi-monodisperse particles at any instant along the vertical axis, $\phi = \phi(z, t)$. The error in the volume fraction has been calculated in terms of the error in the intensity measurement using the uncertainty theory. The model proposed for the volume fraction of particles has an error less than 1% for $\overline{i_n} \leq 0.05$, 0.2% for $0.05 < \overline{i_n} < 0.40$ and 5% for $0.40 < \overline{i_n} < 0.80$. Fig. 3 shows the volume fraction of particles and the mean normalized transmitted light intensity as a function of the vertical axis for different times. This profile, $\phi = \phi(x = L/2, z)$, corresponds to the vertical centerline of the tank for an upright container ($\theta_s = 0.0 \pm 0.5°$), an initial volume fraction $\phi_0 = 5.0 \pm 0.1\%$ and a liquid phase dynamic viscosity of $\eta_{f1} = 6.30 \pm 0.08$ mPa·s. The concentration profiles were calculated from the normalized light intensity using equation (1).

Given the relation between the light intensity and the local concentration, the upper surface of the sediment layer is found by simply identifying the normalized intensity contour where $\overline{i_n} = 0.0435$, corresponding to $\phi \approx 40\%$. The orientation θ_p of the deposit was then determined from the least squares fit of a straight line to the central 10 cm of the tank.

B. Numerical simulations

We have complemented the experiments with a set of two-dimensional numerical simulations using a mixture model. Although numerical models such as dynamic contact, molecular dynamics and discrete elements are capable of capturing more aspects of the interactions between the particles, such techniques are very expensive computationally for dry granular flows, and even more so if considering the interaction with a fluid[33]. Due to the favourable

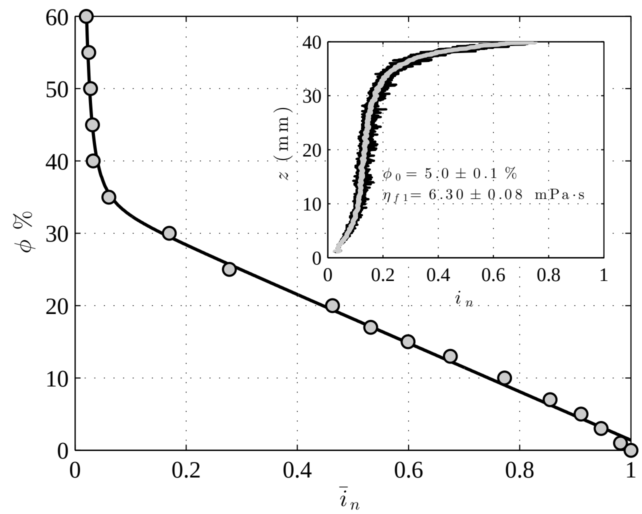

FIG. 2. Experimental calibration curve, showing the volume fraction of particles as a function of the mean normalized transmitted light intensity over the container at $t = 0$, $\overline{i_n} = (1/NM)\sum_j \sum_k i_n(j,k)$. Inset: Mean normalized transmitted light intensity as a function of the vertical axis in a calibration experiment using a vertical container, for a viscosity of $\eta_{f1} = 6.30 \pm 0.08$ mPa·s and an initial volume fraction of $\phi_0 = 5.0 \pm 0.1$ %. The profile corresponds to the final state of the particle sedimentation.

relation between computational accuracy and economy [33,37], we have chosen this continuum approach. The objective of these simulations is two-fold. First, the numerical simulations allowed tracking of the settling process through the concentration and flow velocity output before the final settling condition. Second, the present mixture model does not have a built-in repose angle (or internal friction) condition. Consequently, this model allows us to assess whether or not the internal friction is an important mechanism for setting the final slope of the sediment layer.

The dynamics of the suspension can be modeled by two momentum equations, one for the particles and the other for the fluid, plus a continuity equation for each of the two phases present[11]. Assuming that there is no mass transfer between the two phases, the continuity equations for the continuous and dispersed phase are, respectively, $\partial_t(\rho_f \phi_f) + \boldsymbol{\nabla} \cdot (\rho_f \phi_f \mathbf{u}_f) = 0$ and $\partial_t(\rho_s \phi_s) + \boldsymbol{\nabla} \cdot (\rho_s \phi_s \mathbf{u}_s) = 0$. The subscripts f and s refer to quantities associated with the continuous phase (fluid) and the dispersed phase (solids). In this model, both the continuous and the dispersed phases are considered incompressible and, in the case of the dispersed phase, inelastic. In the present case, particle Reynolds numbers are within

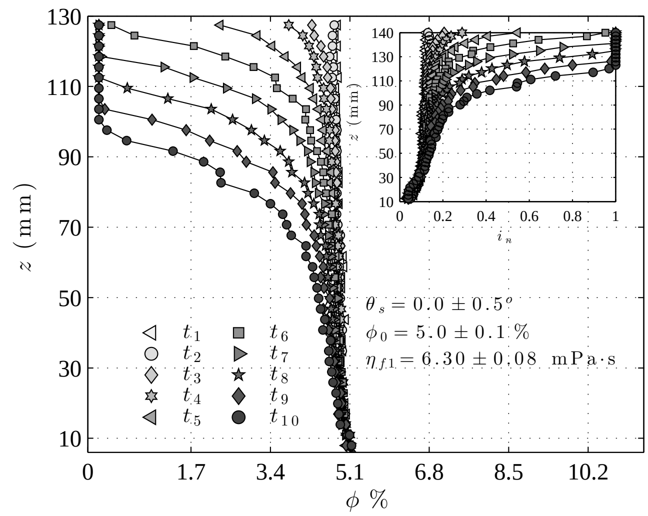

FIG. 3. Volume fraction of particles as a function of the vertical axis for various times. Inset: Mean normalized transmitted light intensity as a function of the vertical coordinate normal to the bottom. Experimental conditions: $\theta_s = 0.0 \pm 0.5°$, an initial volume fraction $\phi_0 = 5.0 \pm 0.1\%$ and a liquid phase dynamical viscosity of $\eta_{f1} = 6.30 \pm 0.08$ mPa·s. The curves correspond, from top to bottom elapsed times between 1 s and 10 s after the start of the experiment, with 1 s increments. The measurements between $z = 0$ and $z = 10$ mm have been discarded due to the reflection of light at the junctions of the acrylic container.

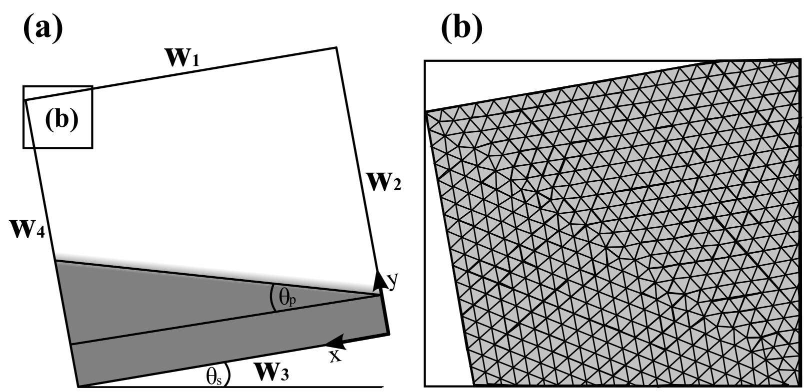

FIG. 4. (a) Computational domain and Boundary conditions. (b) Detail of free triangular mesh used in all numerical simulations (upper left corner).

the Stokes regime, which justifies the incompressibility assumption for both phases. An elasticity hypothesis of the dispersed phase would affect the particle motion after inter-particle collisions and their potential to squeeze fluid out of the sediment layer differently than in the rigid case. Here, as Stokes numbers are very small, all liquid-mediated collisions are indeed inelastic, as discussed below. On the other hand, particle elasticity would alter the loose packing fraction well below the sediment surface, due to the effect of lithostatic pressure. As our experiments and simulations include only relatively shallow particle layers, overburden pressures are not enough to deform the disperse phase at the bottom, thus allowing to plausibly assume that particles are effectively rigid. On the other hand, the intent of the present work is to study particle organization of natural sediments, which are rigid indeed. As the continuous and the dispersed phase are coupled by the total mass conservation requirement, $\phi_f + \phi_s = 1$, the following continuity equation for the mixture is obtained:

$$\boldsymbol{\nabla} \cdot \left(\phi_s \mathbf{u}_s + \mathbf{u}_f \left(1 - \phi_s\right)\right) = 0. \tag{2}$$

The momentum equations for the continuous and disperse phase, using a non-conservative form[12], are, respectively,

$$\rho_f \frac{\partial \mathbf{u}_f}{\partial t} + \rho_f \left(\mathbf{u}_f \cdot \boldsymbol{\nabla}\right) \mathbf{u}_f = -\boldsymbol{\nabla} p + \boldsymbol{\nabla} \cdot \boldsymbol{\tau}_f + \frac{\boldsymbol{\nabla} \phi_f \cdot \boldsymbol{\tau}_f}{\phi_f} + \rho_f \mathbf{g} + \frac{\mathbf{F}_{m,f}}{\phi_f}, \tag{3}$$

$$\rho_s \frac{\partial \mathbf{u}_s}{\partial t} + \rho_s \left(\mathbf{u}_s \cdot \boldsymbol{\nabla}\right) \mathbf{u}_s = -\boldsymbol{\nabla} p + \boldsymbol{\nabla} \cdot \left(\frac{\boldsymbol{\tau}_s}{\phi_s}\right) + \boldsymbol{\nabla} \phi_s \cdot \left(\frac{\boldsymbol{\tau}_s}{\phi_s^2}\right) - \frac{\boldsymbol{\nabla} p_s}{\phi_s} + \rho_s \mathbf{g} + \frac{\mathbf{F}_{m,s}}{\phi_s}. \tag{4}$$

Here, p is the pressure of the mixture, which is assumed equal for both phases, and p_s is a pressure term related to the contribution of the disperse phase to the total pressure, in this case attributed to a purely collisional mechanism, a function ultimately related to the local gradient of the solid fraction and an empirical function mimicking an effective modulus of elasticity, as used in fluidised systems[28].

The viscous stress tensor of each phase is indicated by $\boldsymbol{\tau}$ in the momentum equations and $\mathbf{g}$ is the acceleration due to gravity. The momentum transfer between the phases, $\mathbf{F}_m$, is a volume force exerted upon one of the phases on the other phase. In the momentum equations described above, the continuous phase is considered Newtonian. Hence, the viscous stress tensor is defined as,$\boldsymbol{\tau}_f = \eta_f [\boldsymbol{\nabla} \mathbf{u}_f + \left(\boldsymbol{\nabla} \mathbf{u}_f\right)^T - 2\left(\boldsymbol{\nabla} \cdot \mathbf{u}_f\right) \mathbb{I}/3]$ and $\boldsymbol{\tau}_s = \eta_s [\boldsymbol{\nabla} \mathbf{u}_s + \left(\boldsymbol{\nabla} \mathbf{u}_s\right)^T - 2\left(\boldsymbol{\nabla} \cdot \mathbf{u}_s\right) \mathbb{I}/3]$ [11], where η_f and η_s are the dynamic viscosities of the respective phases and $\mathbb{I}$ is the identity tensor. The dispersed phase requires a viscosity term to model the behaviour of the particles at low and high concentrations. Here, $\eta_s = \eta_f \left(1 - \phi_s/\phi_{s,\max}\right)^{-5/2\phi_{s,\max}}$ is calculated using the model proposed by Krieger and Dougherty[24]. If $\phi_d \to 0$, then $\eta_s = \eta_f$, and if $\phi_s \to \phi_{s,\max}$, then $\eta_s = \infty$.

The interphase momentum transfer is governed by the drag force modelled as $\mathbf{F}_{m,f} = -\mathbf{F}_{m,s} = \beta\left(\mathbf{u}_s - \mathbf{u}_f\right)$, where β is the drag coefficient. In the present set of simulations, the method proposed by Gidaspow[16] for the particle pressure term, and that of Wen and Yu[36] for the drag coefficient for fluids with a high concentration of particles in volume, are considered and detailed in the Appendix V.

The continuity equation of the mixture (2) and momentum transport equations of both phases, (3) and (4), are discretized by the Galerkin finite element method [37]. We have used COMSOL Multiphysics with the CFD package to solve the system of differential equations described above for the experimental conditions of the Table I.

The boundary conditions associated with the computational domain are depicted in Fig. 4(a). First, we consider no-slip conditions and no penetration for both phases in all the domain borders, so that $\mathbf{u}_f = \mathbf{u}_s = \mathbf{0}$ at w_j, with $j \in \{1, ..., 4\}$ (Fig. 4(a)). Regarding the dispersed phase, we imposed a zero-outflow condition in the container, i.e., $\phi_s \mathbf{u}_s \cdot \mathbf{n} = 0$ at w_j. Fig. 4(b) shows the free triangular mesh used in this work for the discretization of the differential equations. In order to choose the appropriate mesh size for the calculations, a set of simulations for different mesh sizes has been performed under three different numerical conditions, $\theta_s = 10°$, $\eta_f = 6.30$ mPa·s and $\phi_0 = 0.05$, 0.10 and 0.20. Fig. 5 shows an example of the sediment layer angle dependence with the number of mesh elements for the case with $\theta_s = 10°$, $\phi_0 = 0.20$ and $\eta_f = 6.30$ mPa·s. We see that the angle of the sediment layer reaches $\theta_p \approx 8°$ with about $10,000$ mesh elements, increasing slightly to $\theta_p = 8.07°$ when $20,000$ mesh elements are used and reaching a constant value $\theta_p = 8.09°$ when over $25,000$ mesh elements are used in the calculations. A compromise between convergence and computational time has been used with $40,000$ triangular elements and a 0.10 s time step for the subsequent calculations. The latter corresponds to 1/4 of the time it takes one sphere to displace its own size at the Stokes settling velocity. Notably, the time step depends on the fluid viscosity, in our case requiring Δt between 0.1 s and 0.2 s. All runs were set to simulate 500 s of real time, thus exceeding the overall bed formation times in the experiments, with output saved every 2 s.

Convergence was assessed when the sediment layer angle, defined as the locus of a solids volume fraction equal 0.40, remained static. This concentration cut-off criterion is justified

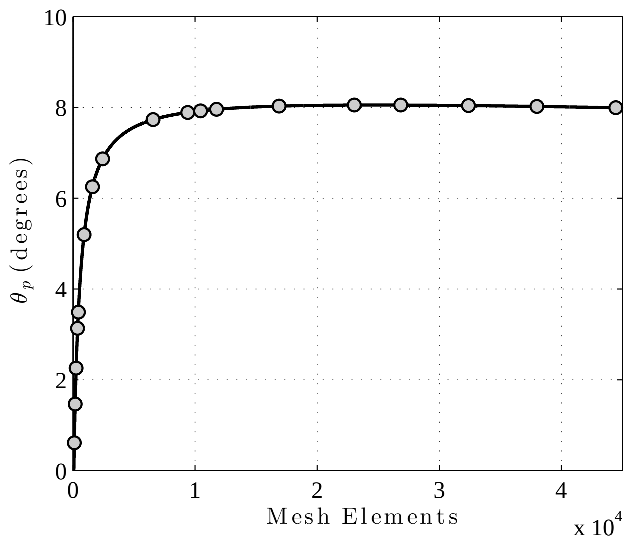

FIG. 5. Convergence of free triangular mesh. θ_p as a function of number of mesh elements. The solid line represents the trend points. Numerical conditions, $\theta_s = 10°$, $\phi_0 = 20\%$, $2\eta_f = 6.30$ mPa·s.

by the abrupt transition predicted by the mixture model at about this value of the particle concentration as the sedimentation progresses for sufficiently long times, as depicted in Fig. 6. The inset in Fig. 6 shows the component of the velocity of particles $\mathbf{u}_s$ parallel to the bottom of the container, for different times. An example showing the computed concentration field and the boundary of the sediment layer below is shown in Fig. 7. The upper, dashed white line in the bottom-right panel represents the sediment layer definition according to the threshold limit for $\phi = 0.40$, defined herein. The grayscale bar represents the concentration of particles.

The set of differential equations and the corresponding initial and boundary conditions used in this work represent a continuum mixture model, and therefore it provides a continuous description of the velocity and particle concentration field. In contrast, when the actual settling process is finished, a discontinuity on the particle concentration field appears at a finite time. This sharp change in the particle concentration may not be captured by the present continuum mixture model in detail. The result of equations (3) and (4) for steady state and the zero-velocity condition represent a hydrostatic particle concentration field, which contradicts the various final angles of the sediment layer found herein. The adjustment of the continuum model from the sloping sediment layer to a hydrostatic state occurs over a much longer time scale than the formation of the bed. The present continuum mixture model is thus only useful during the transient process where the sediment layer is in progress. However, the identification of an abrupt change in the numerical output in the concentration as described above gives a robust and reasonable indication of such a settled condition. This is exposed by comparison with the experimental results in the next section.

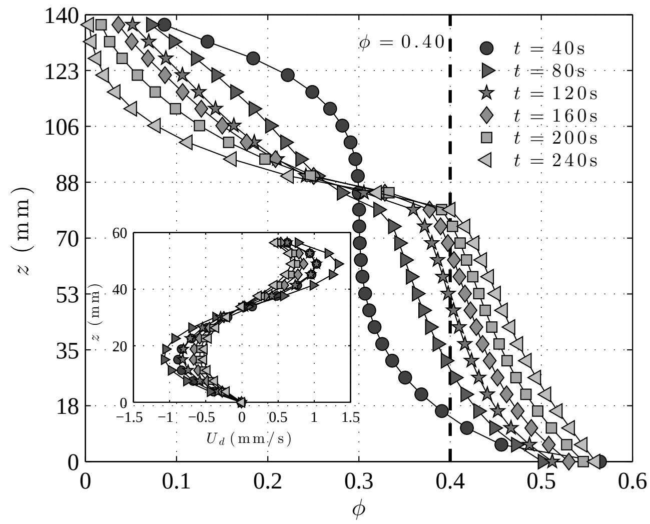

FIG. 6. Particle concentration profile for $\phi_0 = 15.0 \pm 0.1\%$, $\eta_{f1} = 6.30 \pm 0.08$ mPa·s and $\theta_s = 10.0 \pm 0.5°$, measured at $(x = L/2, z)$ for various times. Inset: component of velocity $\mathbf{u}_s$ parallel to the bottom of the container. The vertical, dashed line represents $\phi = 0.4$.

III. RESULTS AND DISCUSSION

A comparison between the experimental and simulated bed formation processes, summarized in Fig. 9, shows an excellent agreement between the experiments and the numerical output. The striking similarity between simulations and experiments suggests that the dominant mechanism of sediment formation is not given by interparticle friction, but by fluid-mediated collisions. The rationale for this conclusion is that while the numerical model determines the pressure in both the continuous (fluid) and discrete (solid) phases, and so determines pressure forces for collision, and determines viscous shear stresses, it does not provide the contact friction associated with settling the angle of repose for dry material. This is consistent with the experimental observation of inelastic collisions for Stokes numbers below about 10, the latter defined by Courrech du Pont et al.[7] as $St = (1/9)[\rho_s(\rho_s - \rho_f)ga^3 \sin(\theta_s - \theta_p)]^{1/2}/\eta_f$, whereas in the present set of experiments the Stokes and particle Reynolds number ranges

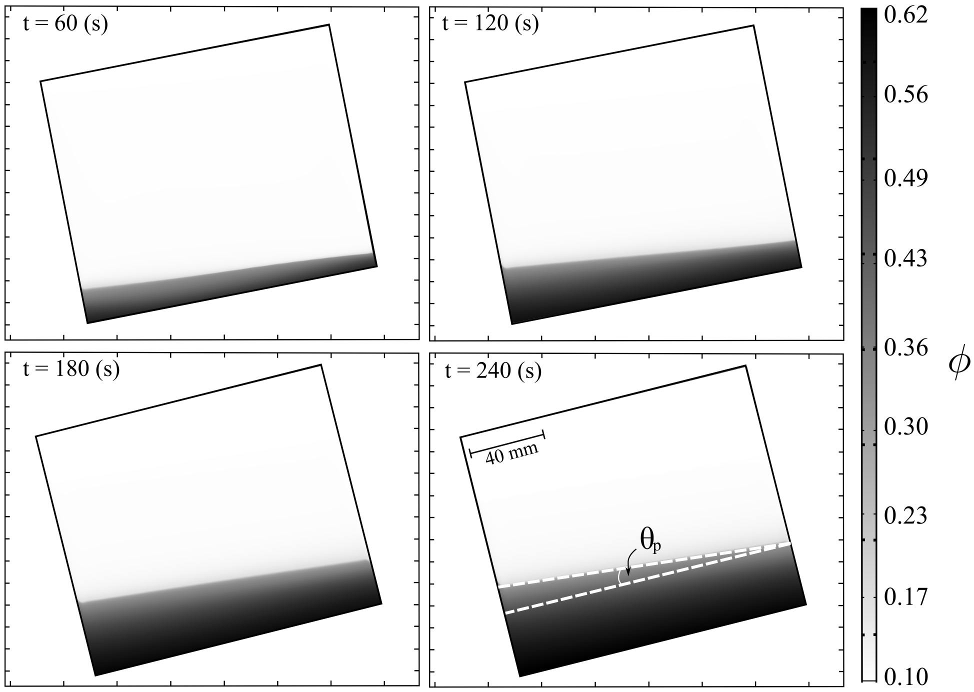

FIG. 7. Particle concentration field obtained from numerical simulations for 60 s, 120 s, 180 s and 240 s. The upper, dashed white line in the bottom-right panel represents the sediment layer definition according to the threshold limit for ϕ, equal 0.40, defined herein. The experimental conditions are the same as shown in Fig. 6. The grayscale bar represents the concentration of particles.

are $0.00721 - 0.001474$ and $0.00370 - 0.03380$, respectively. A consequence of such a particle interaction mode is that there is no available kinetic energy left for bouncing [18,22].

Fig. 10 shows the numerical particle velocity field superimposed on the experimental particle concentration obtained using the light extinction method described above, for an initial volume fraction of $\phi_0 = 0.15$, a viscosity of $\eta_f = 6.30$ mPa·s and two angle system (a) $\theta_s = 0°$ and (b) $\theta_s = 20°$. The numerical simulation predicts velocities below 0.5 mm/s above the sediment layer, whereas within the high concentration zone (extending about 15 mm above the bottom), the velocity is almost zero, indicating the final settled configuration of particles is reached.

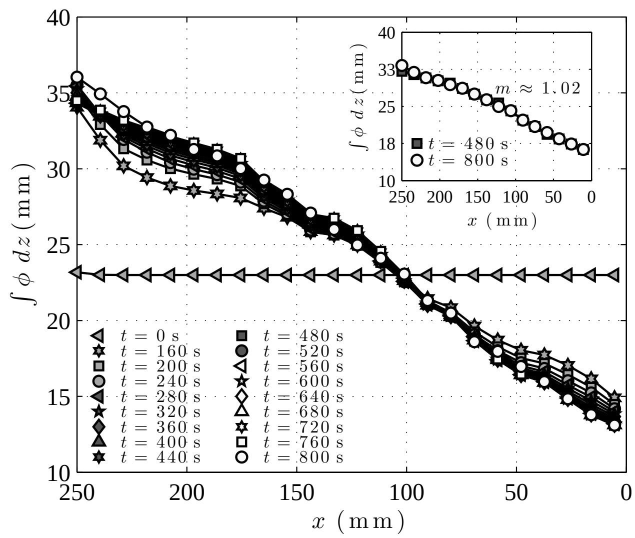

FIG. 8. Accumulated particle mass, $\int \phi(x,z)dz$, as a function of the longitudinal coordinate for different times. Inset: Particle accumulation for long times, with a slope close to $m \approx 1.02$. The corresponding integral has been calculated within the measurement window. Experimental conditions: $\phi_0 = 15.0 \pm 0.1\%$, $\eta_{f1} = 6.30 \pm 0.08$ mPa $\cdot$s and $\theta_s = 10.0 \pm 0.5°$.

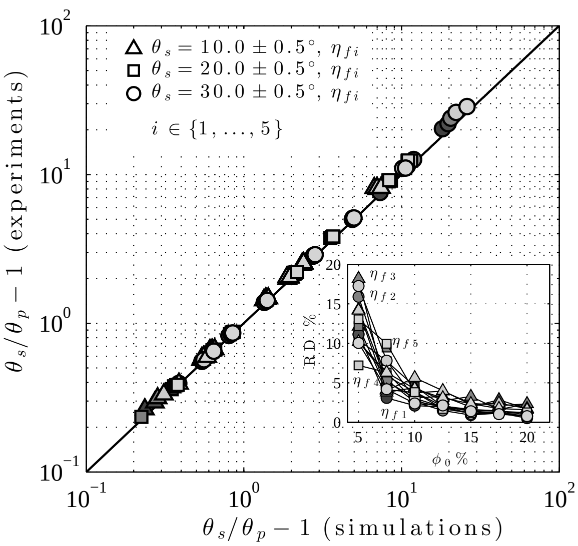

FIG. 9. Comparison between experimental and numerical results. The solid line indicates the identity. Inset: Relative difference (RD %) between experiments and numerical simulations as a function of the initial volume fraction for different viscosities.

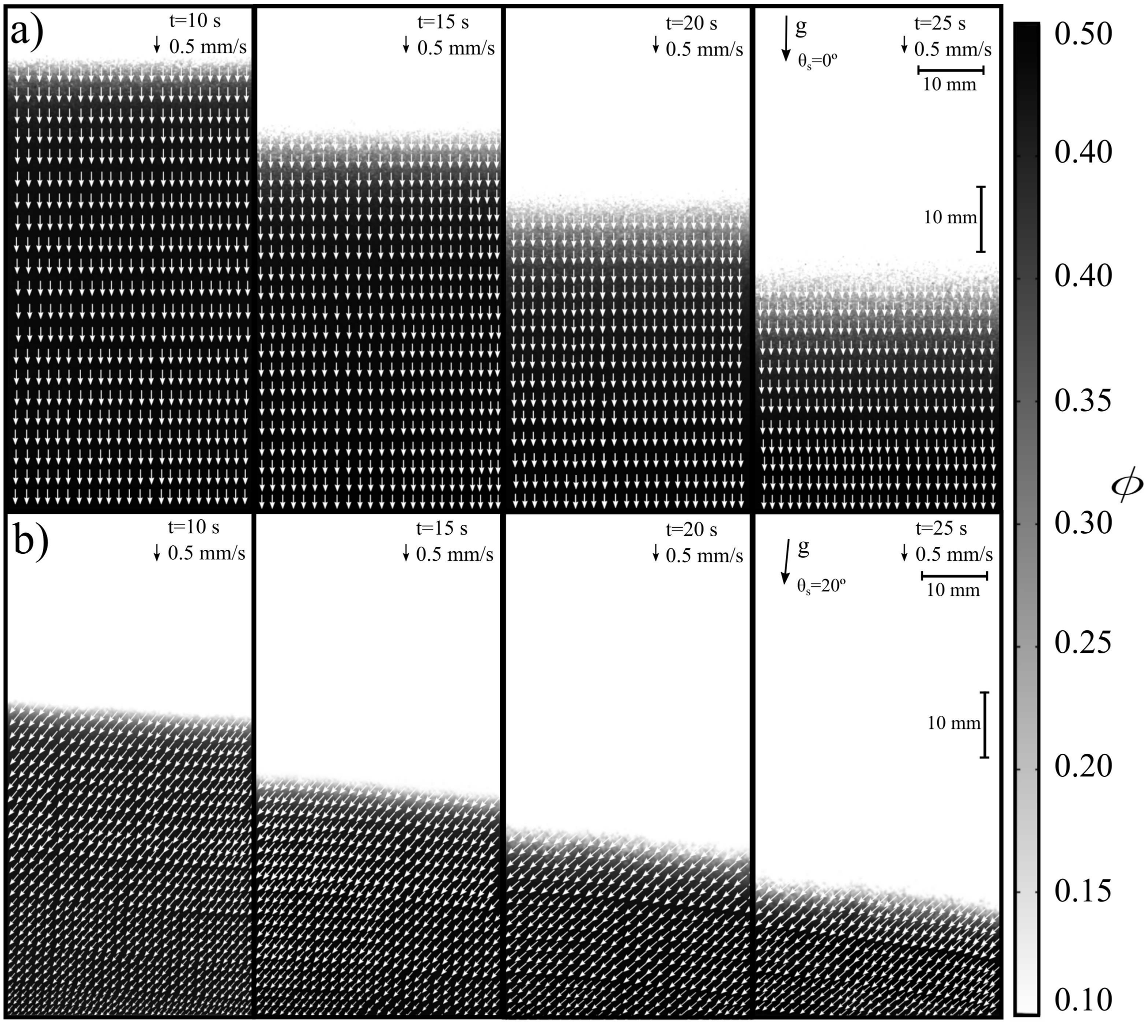

FIG. 10. Evolution of the interface of the suspension, from 10 s to 25 s after the start of the experiment considering a frame of reference aligned with the bottom of the tank. θ_s corresponds to the angle of the bottom of the tank measured from the horizontal plane. The experimental conditions are $\phi_0 = 0.15$, $\eta_f = 6.3 \pm 0.08$ mPa·s for (a) $\theta_s = 0.0 \pm 0.5°$ and (b) $\theta_s = 20.0 \pm 0.5°$. The white arrows represent the computed particle velocity of the disperse phase, $\mathbf{u}_s$ from the numerical simulation for the same experimental conditions.

The particle settling process that forms the sediment layer and controls its final angle is the consequence of three different processes that the particles experience in sequence, as anticipated in Section I. Figure 8 shows that the settling process finally evolves into the formation of a sediment layer, whose upper surface was found to be approximately linear in most of the experiments and simulations. The first process is the quasi-vertical sedimentation of particles (Fig. 11) that drives the linear increase with time seen in the height of the deposit. As particles approach, the sediment layer they contribute to the second process, the formation of a particle flow at a concentration near the packing value. This down-slope flow redistributes the particles towards the lower parts of the container, leading to the observed $\theta < \theta_s$. Additionally, this layer introduces the possibility of some degree of reorganisation due to collisions and local mixture viscosity values[26]. The final settled condition is obtained, with θ less than the angle of repose, after concentration increases and finally the direct contacts among each other render the particles immobile. Despite the existence of velocity fluctuations as predicted by Ham and Homsy[20] (and references therein), for a many-particle interaction process and seen in the velocity fields of Fig. 10, a Kynch-like sedimentation process, where local shearing is not predominant (except by the fluid-particle shearing)[25], gives a good description of the settling. The lower panel shows the sedimentation of quasi-monodisperse particles in a tilted container for different times. As the time passes, the particles begin to settle to the bottom of the container and progressively increase their angle θ_p, measured from the bottom of the container. Unlike the case when the container is upright, once the particles reach the bottom of the container, they start to move down due to the angle of inclination and gravity, until finally the motion ceases because of the increasing concentration of particles and the rapid dissipation of energy from the particle interactions[18,22] and, the final layer of sediment is formed. The dominance of the hindered settling mechanism is shown to fit the experimental concentration profile correction to the settling velocity with the hindrance function proposed by Richardson and Zaki[34], $F = (1 - \phi_0)^n$ (Fig. 12). In addition to the excellent fit between experimental data and this model, the fit parameter ($n = 4.98$) closely resembles the typical value $n \approx 5$ referred in the literature[10,19]. As the resulting dynamics of the sedimentation away from the container bottom (including the velocity fluctuations and particle self-diffusion) has been found to be independent of the container size[19], the details of the flow near the boundaries of the container remain irrelevant for the purposes of the particle dynamics in the interior. The mean height of the sediment layer increases with the bottom plane slope. (Fig. 13). This result is consistent with the trend predicted by Kapoor and Acrivos[23] using boundary layer arguments. As in their work, the present observations show a quasi-linear thickness profile in the range $\phi \in [0.05, 0.20]$. Fig. 14 shows the final angle of the settled layer measured with

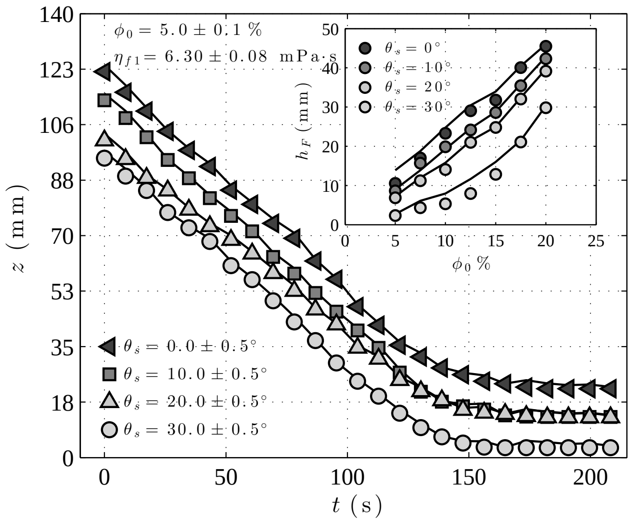

FIG. 11. Time evolution of the height of the interface of the suspension, at $x = L/2$, for various container angles, $\phi_0 = 5\%$ and $\eta_f = 6.30 \pm 0.08$ mPa·s. The black solid lines represent the numerical simulations. Inset: Measured final height of the sediment layer as a function of the initial volume fraction of particles.

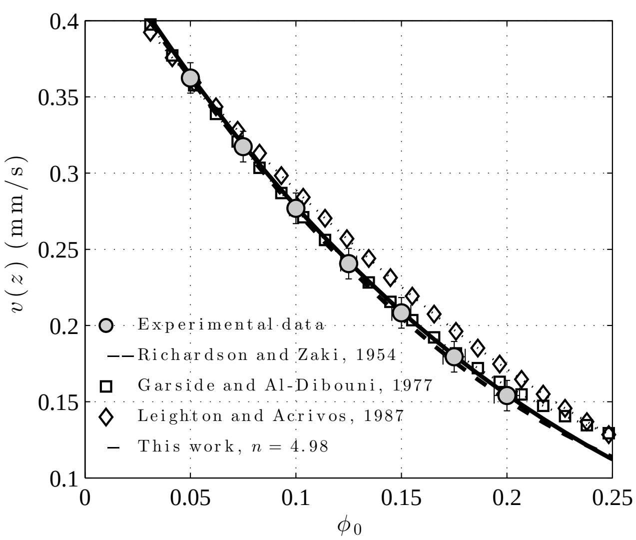

FIG. 12. Velocity of the interface of the suspension, $w_s = w_0(1 - \phi_0)^n$, in terms of the particle concentration. The best fit of the experimental data, using the Richardson-Zaki model corresponds to $n = 4.98$[15,26].

respect to the horizontal, $\theta = \theta_s - \theta_p$, as a function of the initial volume fraction of particles, ϕ_0, for different viscosities, η_f, and container angles of inclination θ_s.

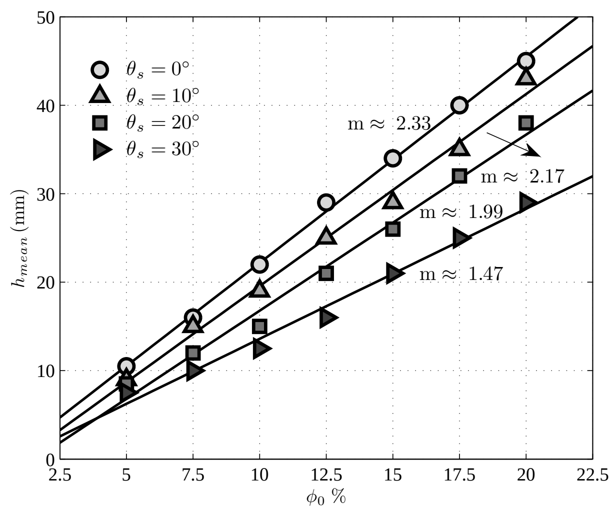

FIG. 13. Mean height of the sediment layer, h_{mean}, as a function of the initial volume fraction and container inclination. The solid lines are for visual aid purposes.

While for the smaller values of θ_s the final angle of the sediment layer tends to change linearly with the initial concentration, at the highest bottom angle, θ tends to decrease more abruptly with concentration. This is explained by both the nonlinearity of the individual particle velocity projection on the bottom slope and the increasingly important effect of the particle concentration on the settling bottom. Fig. 14(a) shows that increasing the initial concentration towards the packing limit causes the difference between the angle of the sediment layer and the container to decrease to zero, implying that the sediment layer evolves to a position parallel to the bottom. An interpretation of this trend is that for initial concentrations approaching the packing limit, the mean free path between particles is on the order of one particle diameter. A time scale for the encounter of two of them, before an inelastic contact occurs, is $4\rho_f a^2/\eta_f$. Assuming that the prevailing energy dissipation precludes the occurrence of interparticle friction, then at volume fractions near the maximum packing fraction, particles tend to end their motion near their starting point, and thus $\theta \to 0$ in this limit. However, for volume fractions much smaller than the packing limit, it is possible to see, in light of the present numerical simulations and experimental results, that the vertical settling stage accounts for a significant part of the overall effect of the particle concentration in the formation of the final angle of the sediment layer. Fig. 14(b) shows that θ is independent of viscosity in the viscous flow experiments range investigated. Courrech du Pont et al.[7] have explained this as the result of the flow of particles for small Stokes numbers.

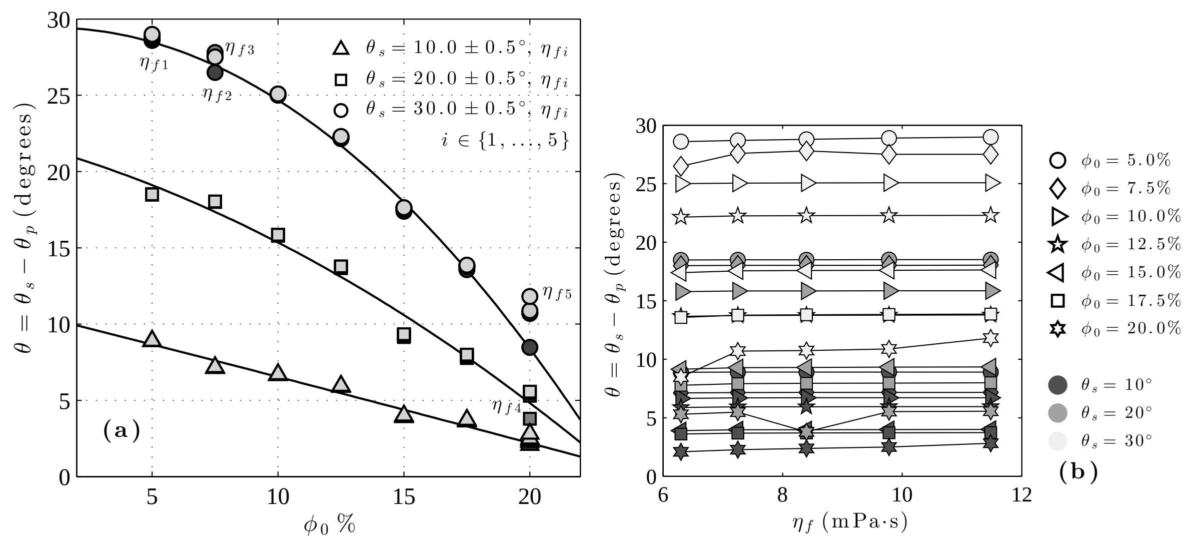

FIG. 14. Final angle of the sediment layer, $\theta = \theta_s - \theta_p$, as a function of: (a) the initial volume fraction and (b) of different viscosities, η_{fi}. The solid lines are for visual aid purposes.

During the final stages of the particle motion, the individual particle momentum decays due to the collisions with their neighbours and due to the interaction with the ambient fluid. This process may be explained following a rheological constitutive model relating particle microscopic rearrangements with the time scale resulting from the (macroscopic) shear rate, modelled by Forterre and Pouliquen[14] (and references therein) as

$$\tau = P\mu(I). \tag{5}$$

Here, τ is the shear stress, P is the pressure and μ is a friction coefficient, expressed in terms of $I = 2a\dot{\gamma}/\sqrt{P/\rho_s}$. The dimensionless variable I can be interpreted as the ratio between two time scales: (a) a microscopic time scale $2a/\sqrt{P/\rho_d}$, which represents the time it takes for a single particle to fall in a hole of size $2a$ under the pressure P and which gives the typical time of rearrangements, and (b) a macroscopic time scale $1/\dot{\gamma}$ related to the mean deformation. Here, $\dot{\gamma}$ is the shear rate and a is the particle radius. It has been recently shown that both (5) and the dimensionless number I are useful not only for characterising dry granular flows, but also for granular flows when the ambient fluid is viscous [4,7]. An example is given by Courrech du Pont et al.[7], where they used a rotating drum geometry to predict the final angle of both dry and liquid-immersed spheres: the corresponding equilibrium angles have been effectively expressed in terms of I using the Stokes number as a means to distinguish whether the particle motion is dominated by gravity, inertia or viscous dissipation. While in the first case the particles keep accelerating, in the last they effectively reach their terminal velocities.

In the present experiments, the spheres fall and feed a dense layer until all the particles are within the sediment layer. A downward motion occurs until the overall system energy is exhausted and a static layer of angle $\theta_s - \theta_p$ is formed. It is observed that a relevant velocity scale in the problem is the sedimentation velocity, $w_s = w_0 F(\phi_0)$ (w_0 is the settling velocity of an individual particle in an infinite medium), with F a hindrance function as described above. In the present flow, the sheared region near the bottom is a few spheres thick, and so the particle radius will be considered as a characteristic length scale. Although during the particle vertical descent phase (before the influence of the inclined bottom) there is no significant shear, the bottom of the container induces some vorticity in its vicinity and a thin, particle-rich layer develops to carry the particles down slope as they sediment onto the sediment layer. In this layer, the shear rate scales with $\dot{\gamma} \sim w_s \sin\theta_s / a$, the settling velocity projection parallel the container bottom. This flowing layer provides a scale for the granular pressure from the immersed weight and projected area of the particles giving $P \sim (4/3) g(\rho_s - \rho_f) a$. The dimensionless parameter I may be then expressed in this viscosity dominated system as $I = Re_p \,(I_0 r)^{1/2} \sin\theta_s$, where $Re_p = 2a\rho_f w_s/\eta_f$ is the usual definition for the particle Reynolds number, $r = \rho_s/\rho_f$ and $I_0 = (3/4)\eta_f^2/\rho_f g(\rho_s - \rho_f)a^3$. In the present set of experiments the particle Reynolds numbers are in the Stokes regime. The weak dependence of the final angle of the sediment layer on the ambient fluid viscosity, along with the fundamental idea in the constitutive model of Cassar et al.[4] that the friction coefficient is a simple function of the dimensionless parameter I, suggests a relation $\mu \sim I = (Re_p \sin\theta_s)^{c_1} (I_0 r)^{\frac{c_2}{2}}$, where for $c_1 = c_2 = 1$ the expression becomes independent of the fluid viscosity within Stokes flow.

Near the bottom, the inertia of the layer flowing down slope is likely to scale with buoyancy. If v_b is the velocity of this layer, then $g(\rho_s - \rho_f) \sim \rho_f v_b^2/\ell$, where the corresponding length scale is taken as the interparticle distance near the bottom, $\ell = 2a(\phi_m/\phi)^{1/3}$

[2,8]. Thus, $\frac{2ag(\rho_s - \rho_f)/\rho_f}{v_b^2} \sim (\phi/\phi_m)^{1/3}$. Again, adding a monomial function to μ yields $\mu \sim (Re_p \sin\theta_s)^{c_1} (I_0 r)^{\frac{c_2}{2}} (\phi/\phi_m)^{\frac{c_3}{3}}$, where this time $c_3 = 1$ reflects the proposed scaling. Fig. 15 shows the best fit for this model in terms of the slope of the final angle of the sediment layer, $\mu = \tan\theta$, and the dimensionless combination $(Re_p \sin\theta_s)^{c_1} (I_0 r)^{\frac{c_2}{2}} (\phi/\phi_m)^{\frac{c_3}{3}}$. The results indicate an excellent fit, with $c_1 = 1.09 \pm 0.01$, $c_2 = 1.03 \pm 0.02$ and $c_3 = 1.11 \pm 0.02$ with a prefactor close to 2.4. The fact that the parameters c_1, c_2 and c_3 are close to the unity confirms that the viscosity does not play a significant role, provided it is high enough to ensure that the particle Reynolds number is well below the unity.

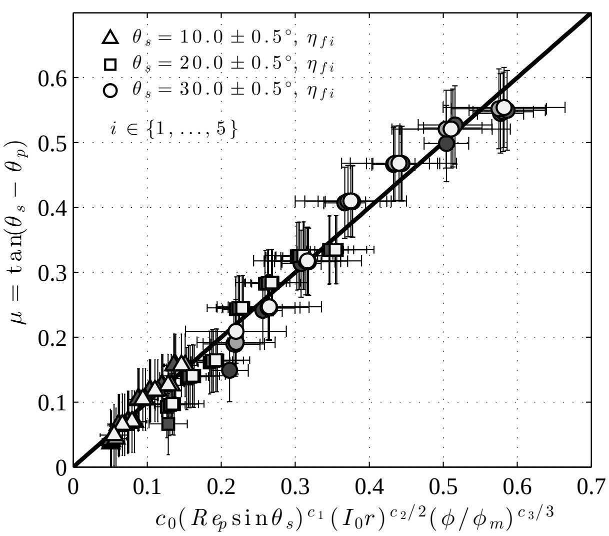

FIG. 15. Data fit for μ as a function of the dimensionless group $(Re_p \sin\theta_s)^{c_1} (I_0 r)^{\frac{c_2}{2}} (\phi/\phi_m)^{\frac{c_3}{3}}$. The solid line indicates the identity.

IV. CONCLUSIONS

The work presented here provides new insight into the mechanism that sets the morphology of the sediment layer formed by the settling of quasi-monodisperse particles onto the bottom of an inclined container. A key finding is that the final angle adopted by the sediment layer shows strong dependencies on the initial particle concentration and the container inclination, but not the fluid viscosity. The idea of hindered settling is central to understanding these results as it allows the formation of a particle-rich layer that advects particles down-slope just above the sediment layer as it forms. Indeed, our results suggest that the result of this mechanism scales directly with the projection of the hindered settling velocity onto the sloping deposit.

While hindered settling depends on viscous forces as well as continuity requirements, the fluid viscosity does not play a direct role in setting the final morphology for low particle Reynolds numbers as it enters the settling velocity $w_s = w_0 F(\phi)$, and consequently the settling flux ϕw_s, only through w_0. Viscosity does, however, control the time scale over which the morphology is established. In contrast, the final state depends strongly on the initial concentration as this enters the settling flux in a nonlinear manner. That fluid-mediated particle interactions (via the hindrance function) dominate over solid friction is demonstrated through our numerical simulations. These simulations that reproduce the experimental results despite using a mixture model that is devoid of any solid friction term and considers the granular material as incompressible. This, in turn, confirms that the dissipation is dominated by viscous forces as the particles approach rather than solid friction after they collide.

Although the present study has been performed in a container with a fixed aspect ratio, it is reasonable to speculate how this may affect the morphology of the sediment layer. For a given initial concentration and container width, increasing the container height will increase the period of time during which the particle-rich layer flows down slope above the developing sediment deposit, and so we would expect the surface of the final deposit to be more horizontal in a manner similar to the decrease in θ seen here by increasing the initial concentration. Conversely, increasing the width of the container (while keeping the height constant) will not significantly alter the down-slope flux while increasing the volume of particles needing to be transported to achieve a given θ. Thus, we would expect θ to increase towards θ_s and the deposit to be of a more uniform thickness (for extreme high or low aspect ratios, the Boycott effect may become important and contribute to the final slope in a manner not described here). Additionally, simply changing the size of the container while maintaining the same aspect ratio will change the time scale over which the sediment layer is created, but not its morphology. Finally, from a practical point of view, these results are important for future application in engineering sciences, specifically in chemical and pharmaceutical industry (e.g., the application of blood cell sedimentation for monitoring of the bioequivalence of drugs based on acetylsalicylic acid), petroleum and mining industry (e.g., transporting of copper concentrates and mining waste), as well as in many kinds of industrial separation processes of granular material from a fluid (e.g., water treatment). In mineral processing, the concentration stage uses water as a carrier fluid for comminution products, where an important part of the fluid is recovered in thickeners. Although the settling mechanism in the mid section of thickeners is vertical, the bottom of these equipment is conical, inducing a particle flow component parallel to the bottom. On the other hand, in the wastewater treatment industry it is common to find lamella settlers, whose working principle is the Boycott effect. Knowing that the final angle adopted by the sediment layer shows strong dependencies on the initial particle concentration and the container inclination, but not the fluid viscosity in this Stokes number range, might improve the design and operation in these examples.

ACKNOWLEDGEMENTS

The authors acknowledge the support of the National Commission for Scientific and Technological Research of Chile, CONICYT, Grant N° 21110766, Fondecyt Projects N° 11110201 and N° 1130910, the Department of Civil Engineering, the Department of Mining Engineering and the Advanced Mining Technology Center of the University of Chile, as well the staff of the G.K. Batchelor Laboratory, Department of Applied Mathematics and Theoretical Physics, University of Cambridge.

V. APPENDIX

To characterize the drag coefficient β for the drag force $\mathbf{F}_{m,f} = -\mathbf{F}_{m,s} = \beta\left(\mathbf{u}_s - \mathbf{u}_f\right)$ in the numerical model, the method proposed by Gidaspow[16] along with the model by Wen and Yu[36] has been used. Specifically,

$$\beta = \begin{cases} \frac{150\eta_f\phi_s^2}{\phi_f d_s^2} + \frac{1.75\phi_s\rho_f\left|\mathbf{u}_{\text{slip}}\right|}{d_s} & \phi_d < 0.20 \\ \\ \frac{3\phi_f\phi_s\rho_f c_D\left|\mathbf{u}_{\text{slip}}\right|\phi_f^{-2.65}}{4d_s} & \phi_s > 0.20, \end{cases} \tag{6}$$

where $\mathbf{u}_{\text{slip}} = \mathbf{u}_s - \mathbf{u}_f$, the diameter of the particles is d_s and c_D is the drag coefficient for a single particle. The drag coefficient is a function of the particle Reynolds number, and is determined from,

$$c_D = \begin{cases} \frac{24}{Re_p}\left[1 + 0.15 Re_p^{0.687}\right] & Re_p < 1000 \\ 0.44 & Re_p > 1000. \end{cases} \tag{7}$$

The particle Reynolds number in the model is defined as $Re_p = \phi_f d_s \rho_f \left|\mathbf{u}_{\text{slip}}\right| / \eta_f$. Finally, for mixtures of particles and fluid, it is necessary to have a model for the solid pressure, p_s in (4). The solid pressure models the particle interaction due to collisions and friction between the solid particles. The implemented approach uses a gradient-based diffusion model expressed as $\boldsymbol{\nabla} p_s = -\chi(\phi_f)\boldsymbol{\nabla}\phi_f$, where the empirical function $\chi(\phi_f)$ has the form $\chi(\phi_f) = 10^{a_1\phi_f + a_2}$. The function $\chi(\phi_f)$ represents the modulus of elasticity for the dispersed phase and has dimensions of pressure in the international system of units[13]. Here, $a_1 = -10.50$ and $a_2 = 9.00$ [17].

REFERENCES

[1]Acrivos, A., Herbolzheimer, E., 1979. Enhanced sedimentation in settling tanks with inclined walls. Journal of fluid mechanics 92 (03), 435–457.

[2]Bagnold, R., 1954. Experiments on a gravity-free dispersion of large solid spheres in a newtonian fluid under shear. Proceedings of the Royal Society of London. Series A: Mathematical and Physical Sciences 225 (1160), 49–63.

[3]Burger, R., Diehl, S., Nopens, I., 2011. A consistent modelling methodology for secondary settling tanks in wastewater treatment. Water Research 45 (6), 2247–2260.

[4]Cassar, C., Nicolas, M., Pouliquen, O., 2005. Submarine granular flows down inclined planes. Physics of Fluids (1994-present) 17 (10), 103301.

[5]Cheng, N.-S., 2008. Formula for the viscosity of a glycerol-water mixture. Industrial and engineering chemistry research 47 (9), 3285–3288.

[6]Concha, F., 2014. Solid-Liquid Separation in the Mining Industry. Springer.

[7]Courrech du Pont, S., Gondret, P., Perrin, B., Rabaud, M., 2003. Granular avalanches in fluids. Physical Review Letters 90 (4), 044301.

[8]Coussot, P., Ancey, C., 1999. Rheophysical classification of concentrated suspensions and granular pastes. Physical Review E 59 (4), 4445.

[9]Dalziel, S. B., 2012. DigiFlow User Guide. Version 3.4. Dalziel Research Partners.

[10]Davis, R. H., Acrivos, A., Jan 1985. Sedimentation of noncolloidal particles at low reynolds numbers. Annual Review of Fluid Mechanics 17 (1), 91–118.

[11]Enwald, H., Peirano, E., Almstedt, A. E., Dec 1996. Eulerian two-phase flow theory applied to fluidization. International Journal of Multiphase Flow 22, 21–66.

[12]Ergun, S., 1952. Fluid flow through packed columns. Chemical Engineering Progress 48, 89–94.

[13]Ettehadieh, B., Gidaspow, D., Lyczkowski, R., 1984. Hydrodynamics of fluidization in a semicircular bed with a jet. AIChE journal 30 (4), 529–536.

[14]Forterre, Y., Pouliquen, O., 2008. Flows of dense granular media. Annu. Rev. Fluid Mech. 40, 1–24.

[15]Garside, J., Al-Dibouni, M. R., 1977. Velocity-voidage relationships for fluidization and sedimentation in solid-liquid systems. Industrial and engineering chemistry process design and development 16 (2), 206–214.

[16]Gidaspow, D., 1994. Multiphase Flow and Fluidization: Continuum and Kinetic Theory Descriptions. Academic Press.

[17]Gidaspow, D., Shih, Y.-T., Bouillard, J., Wasan, D., 1989. Hydrodynamics of a lamella electrosettler. AIChE journal 35 (5), 714–724.

[18]Gondret, P., Lance, M., Petit, L., 2002. Bouncing motion of spherical particles in fluids. Phys. Fluids 14 (2), 643–652.

[19]Guazzelli, E., Hinch, J., Jan 2011. Fluctuations and instability in sedimentation. Annual Review of Fluid Mechanics 43 (1), 97–116.

[20]Ham, J., Homsy, G., 1988. Hindered settling and hydrodynamic dispersion in quiescent sedimenting suspensions. International Journal of Multiphase Flow 14 (5), 533–546.

[21]Herbolzheimer, E., Acrivos, A., 1981. Enhanced sedimentation in narrow tilted channels. Journal of Fluid Mechanics 108, 485–499.

[22]Joseph, G., Zenit, R., Hunt, M., Rosenwinkel, A., 2001. Particle–wall collisions in a viscous fluid. Journal of Fluid Mechanics 433, 329–346.

[23]Kapoor, B., Acrivos, A., 5 1995. Sedimentation and sediment flow in settling tanks with inclined walls. Journal of Fluid Mechanics 290, 39–66.

[24] Krieger, I. M., Dougherty, T. J., 1959. A mechanism for non-newtonian flow in suspensions of rigid spheres. T. Soc. Rheol. 3, 137–152.

[25] Kynch, G., 1952. A theory of sedimentation. Transactions of the Faraday Society 48, 166–176.

[26] Leighton, D., Acrivos, A., 9 1987. The shear-induced migration of particles in concentrated suspensions. Journal of Fluid Mechanics 181, 415–439.

[27] Leung, W. F., Probstein, R. F., 1983. Lamella and tube settlers. 1. model and operation. Industrial & Engineering Chemistry Process Design and Development 22 (1), 58–67.

[28] Massoudi, M., Rajagopal, K., Ekmann, J., Mathur, M., 1992. Remarks on the modeling of fluidized systems. AIChE Journal 38 (3), 471–472.

[29] More, J. J., 1978. The Levenberg-Marquardt algorithm: implementation and theory. Springer.

[30] Nir, A., Acrivos, A., 3 1990. Sedimentation and sediment flow on inclined surfaces. Journal of Fluid Mechanics 212, 139–153.

[31] Peacock, T., Blanchette, F., Bush, J. W. M., Apr. 2005. The stratified Boycott effect. Journal of Fluid Mechanics 529, 33–49.

[32] Phillips, R. J., Armstrong, R. C., Brown, R. A., Graham, A. L., Abbott, J. R., Jan 1992. A constitutive equation for concentrated suspensions that accounts for shear induced particle migration. Physics of Fluids A: Fluid Dynamics 4 (1), 30–40.

[33] Poschel, T., Schwager, T., 2005. Computational granular dynamics: models and algorithms. Springer Science & Business Media.

[34] Richardson, J., Zaki, W., Dec 1954. Sedimentation and fluidisation: Part i. Chemical Engineering Research and Design 32, S82–S100.

[35] Shaqfeh, E. S. G., Acrivos, A., 1986. The effects of inertia on the buoyancy-driven convection flow in settling vessels having inclined walls. Physics of Fluids 29 (12), 3935–3948.

[36] Wen, C., Yu, Y., 1966. Mechanics of fluidization. Chemical Engineering Progress Symposium Series. 62, 100–110.

[37] Zienkiewicz, O. C., Taylor, R. L., Nithiarasu, P., 2013. The Finite Element Method for Fluid Dynamics, Seventh Edition. Butterworth-Heinemann.